

Full length article

Anisotropic degradation mechanism on low-velocity impact of 3D braided composites after thermo-oxidative ageing

Yuanyuan Wu, Jinhui Guo, Limeng Xun, Baozhong Sun, Bohong Gu *

Shanghai Frontier Science Research Center for Modern Textiles, College of Textiles, Donghua University, Shanghai, 201620, China

ARTICLE INFO

Keywords:

Braided composites
Environmental degradation
Impact behavior
Damage tolerance

ABSTRACT

Anisotropic mechanical behaviors are the most prominent feature of 3D braided composites compared with homogeneous materials. This study reports anisotropic low-velocity impact behaviors of 3D braided carbon fiber/epoxy composites along in-plane (IP) and out-of-plane (OP) directions after thermo-oxidative ageing. The stress-strain responses, local strain and damage evolution were obtained. The stress distribution of each yarn and the interface damage propagation were analyzed with numerical analysis method. The retention rate of peak stress of 94.4% and elastic modulus of 91.45% along OP direction are greater than those along IP direction, which are 76.21% and 71.27% respectively. It reveals that the OP direction loading has a better performance on resistance ageing degradation than that in IP loading, and the stiffness degradation is more sensitive. There are X-shape shear damages along OP direction, and interior damages in surrounding area and yarn path along IP direction. Furthermore, the tight braided structure contributed to resisting degradation of mechanical properties along IP direction.

1. Introduction

Three-dimensional (3D) braided composites will be inevitably subjected to various external stresses and harsh environment during service process in fields of aviation, transport, and marine vessels, especially dynamic impact and thermo-oxidative ageing conditions [1–3]. The residual mechanical strengths will be degraded in high temperature and oxygen environment for a period of time because of matrix degradation, interface debonding and matrix cracking [4,5]. The 3D braided composites have different mechanical behaviors after thermo-oxidative ageing owing to the braided structure complexity [6–9], which will cause the anisotropic behaviors when loading in different directions. It will further affect the lifetime and security of structure parts in their service. Therefore, it is necessary to study the anisotropic degradation of composites for structure design.

Many researches have revealed the mechanical behaviors of braided composites when loading along different directions without thermal oxygen ageing treatment. For in-plane (IP) or longitudinal impact, the matrix cracking and interface debonding are the main failure modes. After the stress reaching up peak point, the braided reinforcement will bear loading with stress decreasing. In out-of-plane (OP) or through-thickness direction, the shear failure including fibers breakage, sliding and distortion occupies the principal mode [10–12]. In transverse direction, the major damage and failure modes contain resin crushing, fiber slip and shear failure. When the composites are exposed to the heat

and oxygen environment, the damages including matrix cracks and interface debonding only occur on the cross-section of axial direction and develop to inside along yarn direction [13]. That will lead to mechanical degradation difference when composites are loaded in different directions. Mourid et al. [14], Zuo et al. [15] and Li et al. [7] have proved that ageing cracks will induce anisotropic degradation in quasi-static tensile and compressive behaviors. Low-velocity impact (LVI) is very common during the service life of composite structures [16–21]. However, the LVI anisotropic degradation mechanism of 3D braided composite caused by thermo-oxidative ageing has not been studied.

This study reports anisotropic degradation mechanism on the LVI behaviors of three-dimensional four-directional (3D4d) braided composites after ageing along IP and OP directions with numerical and experimental methods. The global and local evolution processes of damages and strain were shown using high-speed camera and digital image correlation (DIC) techniques. The spatial stress and interface damages distributions were analyzed using mesoscale finite element analysis (FEA) method. In addition, the effects of braided angle on ageing residual strength and stiffness were also discussed. It provided a detailed comprehension for ageing effects on directional mechanical behaviors of braided composite structures.

* Corresponding author.

E-mail address: gubh@dhu.edu.cn (B. Gu).

Table 1
The mechanical properties of carbon fiber, yarn and epoxy resin [23].

	E_{11} (GPa)	$E_{22} = E_{33}$ (GPa)	$G_{12} = G_{13}$ (GPa)	G_{23} (GPa)	$\nu_{12} = \nu_{13}$	ν_{23}	Density (g/cm ³)
Epoxy resin	2.4		0.89		0.35		1.13
Carbon fiber	230	14	9	5	0.25	0.3	1.8
Unaged yarns	169.49	7.34	3.59	2.79	0.25	0.33	1.62
Aged yarns	169.49	6.85	3.59	2.81	0.25	0.31	1.62

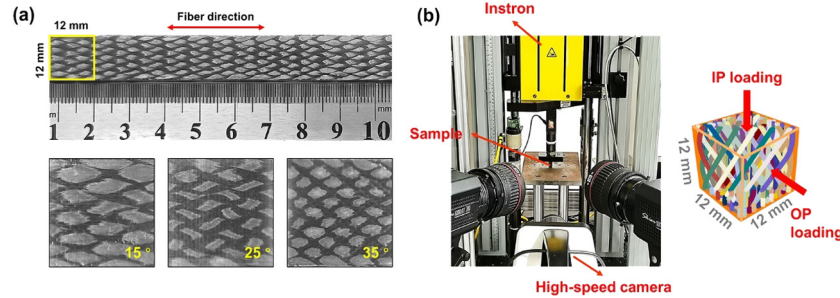


Fig. 1. Samples and testing conditions. (a) 3D braided composites with different angles, (b) loading apparatus under in-plane (IP) and out-of-plane (OP) directions.

2. Composite samples preparations and tests

2.1. The braided composite preparation and ageing treatment

The 3D4d braided composites in Fig. 1(a) with 15°, 25°, 35° braided angles were prepared with SYT49S-12K carbon fiber tows (Zhongfu Shenying Carbon Fiber Co., Ltd, China) and JC-02A/JC-02B epoxy resin (Changshu Jiafa Chemical Inc, China) using vacuum assisted resin transfer molding technique. Table 1 shows the mechanical properties of raw materials of carbon fiber and epoxy resin. The rectangular integrated preforms were prepared with 1*1 four-step braiding method [22], which included 121 body yarns and 22 side yarns. The curing was conducted in an oven with 90 °C for 2 h, 110 °C for 1 h and 130 °C for 4 h. The samples were cooling down at room temperature and cut into about 12*12 *12 mm cubes for testing. The fiber volume fractions of 15°, 25°, 35° composites, which tested with combustion method at 450 °C for 4 h, were 35.6%, 36.4%, and 38.7%, respectively.

The isothermal accelerated ageing method was used to deal with samples, where ageing temperature was 180 °C which was above glass transition point of composites (~130 °C). The composite system in this paper will damage after ageing for 4 days according to our previous studies [13]. Therefore, the ageing treatment was conducted in an isothermal oven for 16 days at 180 °C.

2.2. Tests

2.2.1. LVI loading

The cross-sections of unaged and aged composites were grinded and polished before impact test for obtaining regular surface. The LVI tests of composites were conducted on Instron Dynatup 9250 along IP and OP directions with 25 J impact energy at room temperature (shown in Fig. 1(b)). The specimens could be labeled as 'ab-180-c', where a, b and c represented braided angle (15°, 25°, 35°), impact directions (IP, OP) and ageing days (0, 16), respectively. Each test was repeated three times to obtain the average results. The stress-strain curves have been obtained. Moreover, the retention rates of mechanical properties including peak stress, elastic modulus and absorbed energy were calculated according to the equation of $\frac{P_a}{P_u}$. P_a is the mechanical properties of the aged composites, and P_u is the corresponding values of the unaged samples. They signify the abilities to resist the mechanical property degradation inducing by thermal oxygen ageing. The greater the retention rate values, the better the resistance abilities. The high-speed camera (i-Speed 716, IX Cameras Ltd, UK) was used to record damage and failure evolution processes with a 10,000 frames per

second and 800,000 pixels. In addition, the optical microscope and SEM were used to observe surface micromorphology.

2.2.2. Digital image correlation progressing

The high-quality, flexible and openly available 2D digital image correlation (2D-DIC) software package [24] was used to calculate and show strain field changes in three directions of x , y and xy (defined as E_{xx} , E_{yy} , and E_{xy}). Before testing, the white paint was sprayed all over the testing surface by airbrush. After drying, the random speckles formed by black paint were sprayed on it. During this operation, the same spray distance and times were controlled to avoid error. The high-speed camera was used to record the whole deformation process.

3. Results and discussion

3.1. Impact responses

3.1.1. Anisotropic degradation behaviors under IP and OP directions

Fig. 2 shows stress-strain curves, stiffness, absorbed energy and retention rate behaviors of unaged and aged composites with 15° braided angle along IP and OP directions at 25 J impact energy. It is found that both of the stresses along IP and OP directions show nonlinear increase before reaching ultimate strength with the strains increase. Then the stresses decrease to zero with the strains decrease, which exhibits a rebound state due to smaller damages (shown in Section 3.4). The residual energy was stored in samples and converted to elastic energy, and to bounce it back [25]. The resin matrix occurred degradation and shrinkage under the combined effects of high temperature and oxygen, which caused by chemical bond breakage and rearrangement, volatilization of small molecule species. In addition, the difference of thermal expansion performance between carbon fibers and resin also resulted in interfacial debonding. These factors have affected the mechanical performance of composites when impact along different directions. The close-up view at the linear portion of the stress-strain curves, in which the slope of each fitted line means the elastic modulus or stiffness, is shown in Fig. 2(b). The labeled data near the lines are the elastic modulus values. The stress and stiffness of the aged samples degrade, and the values of maximum strain, plastic strain and absorbed energy increase (Fig. 2(a–c)) compared with those of the unaged composites. For the IP impact, the larger energy absorption of the aged composite is from the more damages and larger strain occurred, while it mainly arises from more deformation for OP impact (shown in Section 3.4). The more serious damages contributed to obtain the more energy absorption in the aged composites. Table 2 and Fig. 2(d) list the

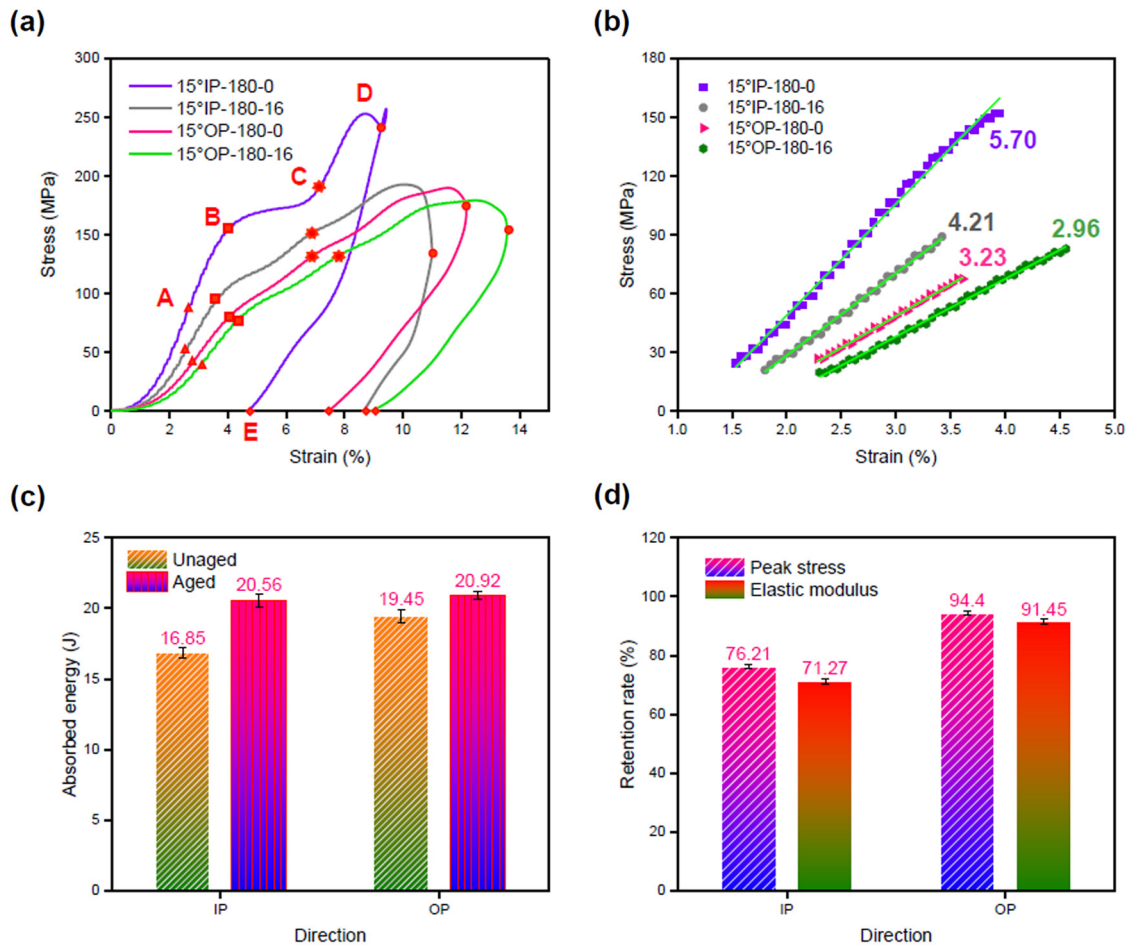


Fig. 2. Stress-strain, stiffness, absorbed energy and retention rate of unaged and aged composites along IP and OP loading directions, (a) stress-strain curves, (b) the close-up view at the linear portion of the stress-strain curves, (c) absorbed energy, (d) retention rate of peak stress and elastic modulus.

specific values and retention rate values at the two loading conditions. The retention rate of peak stress of 94.4% and elastic modulus of 91.45% along OP direction are greater than those along IP direction, which are 76.21% and 71.27% respectively. These data indicate that it has a greater effect on ultimate strength and stiffness degradation in IP than that in OP, which suggests that there is anisotropic degradation of the LVI behaviors in the 3D4d braided composites after ageing. The existed ageing cracks propagating along fiber direction accelerated the damages development when the loading direction was in-plane. The peak stress retention rate values are greater than elastic modulus in both loading conditions. This phenomenon indicate that the stiffness is more sensitive to high-temperature ageing, which is also reasonable for other impact energies in composites with 25° such as 5 J and 15 J [26]. Moreover, the values of the ultimate strength and the elastic modulus along IP direction are greater than those of the OP direction, and the strain values are lower. The axial direction of fiber bore the more capacity when impacted the composites along IP direction at the same conditions, which caused the better mechanical performance.

3.1.2. Effect of the braided angle

Fig. 3 shows strength, stiffness, absorbed energy and retention rate behaviors of 3D braided composites with 15°, 25° and 35° angles along IP directional impact under LVI loading at 25 J. The nonlinear behaviors of stress-strain curves in 25° and 35° samples before peak stress are the same with those of the 15° sample (Fig. 3(a)). Then the stress starts to decrease with the increase of strain. Unlike the rebounded state in 15° sample, the strains in the 25° and 35° samples continue to increase until the end. That presents penetration state due

Table 2

The specific values of composites with different surface braided angles under different loading directions.

Sample	Peak stress (MPa)	Plastic strain (%)	Elastic modulus (GPa)	State
15°IP-3D180-0	253.20	4.73	5.70	Rebounded
15°IP-3D180-16	192.97	8.65	4.21	
15°OP-180-0	190.10	7.46	3.23	
15°OP-180-16	179.46	8.90	2.96	
25°IP-3D180-0	154.68	16.40	4.60	Penetration
25°IP-3D180-16	121.90	30.68	3.30	
35°IP-3D180-0	115.99	16.12	3.70	
35°IP-3D180-16	106.32	22.20	2.73	

to more damages such as resin cracking, interface debonding, and fiber tow buckling and slipping as shown in Section 3.3. The peak stress and elastic modulus decrease with the increasing of the braided angle. The mechanical properties of the aged composite show the degradations of the three braided-angle samples (Table 2 and Fig. 3(b, c)). In the unaged composites, the absorbed energy increases with the increasing of the braided angles. In the smaller angle composites (15°), the composites have the lesser damages. The energy absorption is mainly from the lesser damages and plastic deformation. In the larger angle composites (25° and 35°), the component of force in the fiber direction reduced. Whereas the force in the transverse direction which can promote the slip between the crossed yarns increased. Therefore, the impact strength decreased in the larger angle composites, which was bad for energy absorption. Also, the tighter structure and the more yarn tangles of 35° composites had more carrying capacity after damages

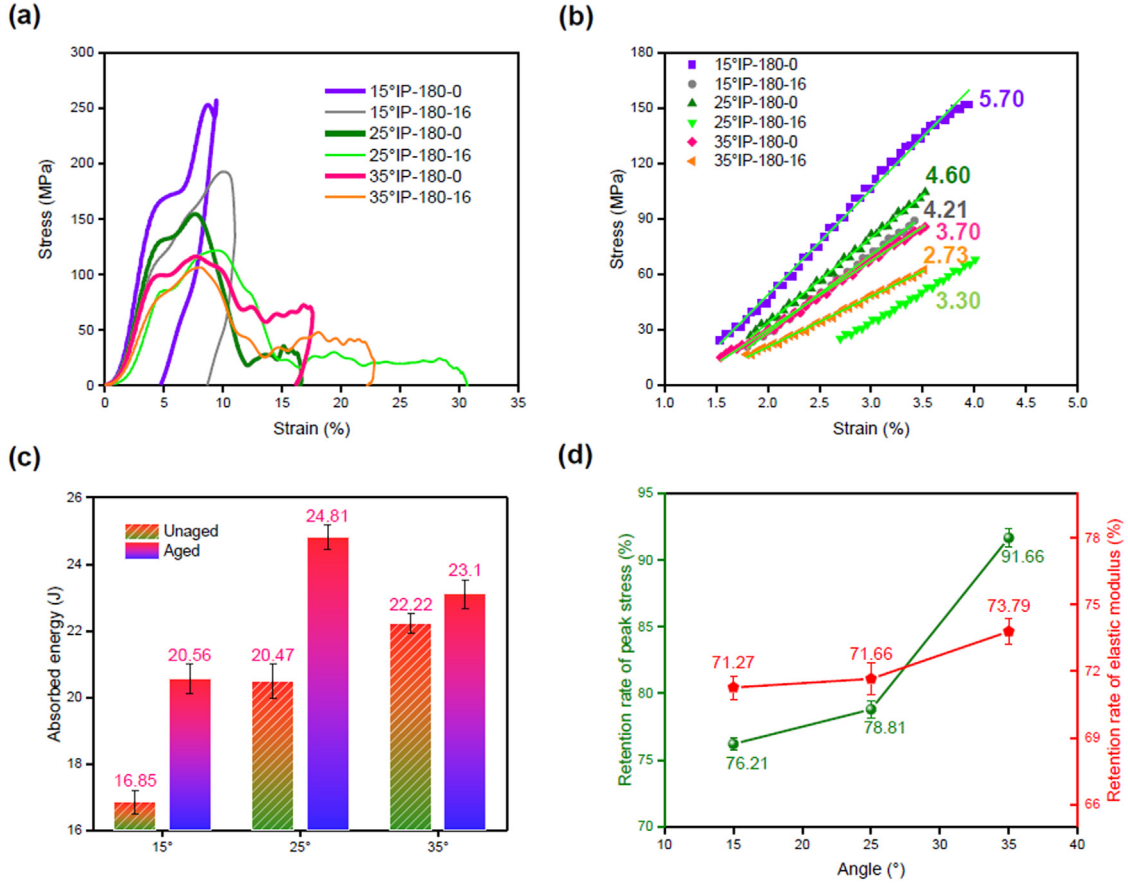


Fig. 3. Stress-strain, stiffness, absorbed energy and retention rate of unaged and aged composites with 15°, 25° and 35° braided angles along IP loading, (a) stress-strain curves, (b) the close-up view at the linear portion of the stress-strain curves, (c) absorbed energy, (d) retention rate of peak stress and elastic modulus.

(Fig. 3a), which was beneficial to energy absorption. The last results were the balance of the two cases. Interestingly, the values of plastic strain and energy absorption of the aged composites increase first and then decrease with the increasing of braided angles. During ageing, the ageing cracks propagated along fiber direction, which resulted in the more serious deformation and damages when these aged samples were impacted along in-plane direction (fiber direction). However, the tighter structure and the more yarn tangles of 35° composites helped reduce the damages and deformation, which was adverse to the energy absorption. Therefore, the energy absorption in the aged composites with 35° was lower than that in the 25° composites. Furthermore, the peak stress retention rates of 76.21%, 78.81% and 91.66%, which corresponding to 15°, 25°, 35° respectively, are greater than elastic-modulus retention rates of 71.27%, 71.66% and 73.79%, respectively (Fig. 3(d)). It manifests that stiffness is also more sensitive than ultimate strength in different braided-angle composites under ageing environment. Furthermore, the retention rate values are positively correlated with angle. It indicates that the 3D braided composites with the compact structure have higher retention rate of mechanical behaviors after ageing.

3.2. Stress and damage distribution during impacting

3.2.1. Numerical modeling and validation

The mesoscopic geometric model, which includes fiber tows (yarns) and resin, were used to analyze stress and damage distribution of the unaged and the aged composites samples along IP and OP loadings. The yarns were regarded as transversely isotropic unidirectional composites including carbon fibers and resin, in which cross-section shapes were regular hexagon [23,27]. Fig. 4 shows sketch of modeling process using CATIA V5R20 software. The numerical calculation

was conducted on commercial finite element analysis (FEA) software. According to the relationship between initial velocity and impact energy [28], a 2625 mm/s pre-velocity was implemented on impact plate. The boundary conditions were shown in Fig. 4.

The material properties were defined using elastic-plastic constitutive model which is valid for mechanical property prediction including quasi-static and impact of 3D braided composites [4,29,30]. Because the resin was isotropy solid, it obeyed J2 hardening plasticity theory and von Mises yield criterion [31]. The input parameters of elastic and plastic properties were derived from experimental tests. Fig. 5(a) shows the nominal (Nom) and true (True) stress-strain of the unaged and aged neat epoxy under LVI loading at 25 J. The true stress (σ_{true}) and strain (ϵ_{nom}) can be calculated from Eqs. (1) and (2). The true elastic moduli of the unaged and the aged composites were 2.07 GPa and 1.82 GPa respectively. The yield stress and plastic strain data (Fig. 5(b)) were extracted from $\sigma_{true} - \epsilon_{true}$ curves.

$$\sigma_{true} = \sigma_{nom}(1 + \epsilon_{nom}) \quad (1)$$

$$\epsilon_{true} = \ln(1 + \epsilon_{nom}) \quad (2)$$

Moreover, Huang's bridging model [32] and Hill's plasticity model were used to define the elastic and plastic properties of equivalent yarns. The relationship of compliance matrix among yarns [S_y], resin [S_m] and fibers [S_f] could be referred to Eq. (3).

$$[S_y] = \frac{V_f [S_f] + V_m [S_m] [A]}{V_f [I] + V_m [A]} \quad (3)$$

The V_f , V_m , $[A]$, $[I]$ are the volume fractions of fiber and resin which were 73.5% and 27.5% respectively, the bridging matrix, and the unit matrix. The elastic parameters of equivalent yarns as shown in Table 1

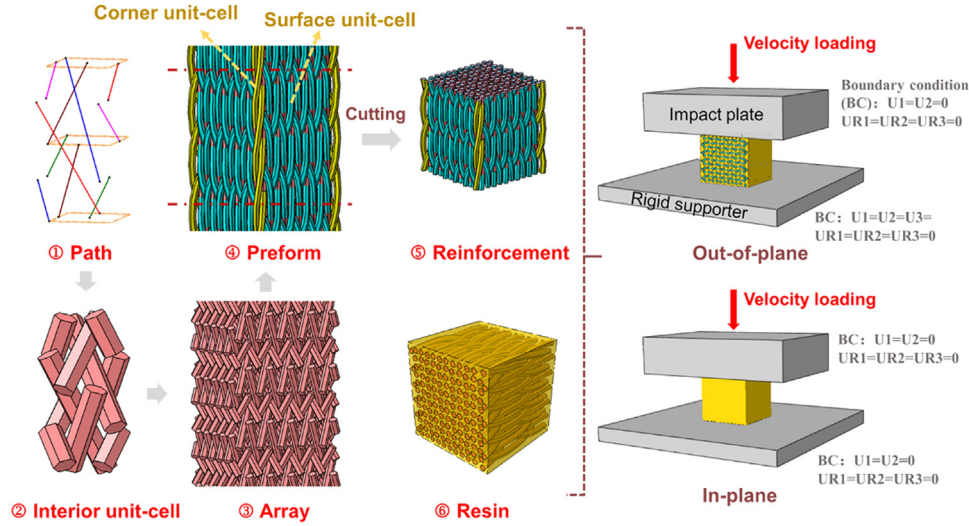


Fig. 4. The sketch of meso-scale geometric model.

Table 3

The yield stress ratio R_{ij} in Hill potential function of yarns in unaged and aged composites in FEA.

	R_{11}	R_{22}	R_{33}	R_{12}	R_{13}	R_{23}
Yarn- unaged	28.58	1	1	0.8	0.8	1.07
Yarn- aged	28.58	0.86	0.86	0.66	0.66	0.91

The Hill potential function of the equivalent yarns is shown in Eqs. (4) and (5).

$$f(\sigma)^2 = F(\sigma_{22} - \sigma_{33})^2 + G(\sigma_{33} - \sigma_{11})^2 + H(\sigma_{11} - \sigma_{22})^2 + 2L\sigma_{23}^2 + 2M\sigma_{31}^2 + 2N\sigma_{12}^2 \quad (4)$$

$$F = \frac{1}{2} \left(\frac{1}{R_{22}^2} + \frac{1}{R_{33}^2} - \frac{1}{R_{11}^2} \right)$$

$$G = \left(\frac{1}{R_{33}^2} + \frac{1}{R_{11}^2} - \frac{1}{R_{22}^2} \right)$$

$$H = \left(\frac{1}{R_{11}^2} + \frac{1}{R_{22}^2} - \frac{1}{R_{33}^2} \right) \quad (5)$$

$$L = \frac{3}{2R_{23}^2}$$

$$M = \frac{3}{2R_{13}^2}$$

$$N = \frac{3}{2R_{12}^2}$$

Therein, R_{ij} is yield stress ratio in all directions, i.e., $R_{11} = \frac{\bar{\sigma}_{11}}{\sigma^0}$, $R_{22} = \frac{\bar{\sigma}_{22}}{\sigma^0}$, $R_{33} = \frac{\bar{\sigma}_{33}}{\sigma^0}$, $R_{12} = \frac{\bar{\sigma}_{12}}{\tau^0}$, $R_{13} = \frac{\bar{\sigma}_{13}}{\tau^0}$, $R_{23} = \frac{\bar{\sigma}_{23}}{\tau^0}$. $\bar{\sigma}_{ij}$ and σ^0 are the nonzero yield stress and reference yield stress values respectively. $\tau^0 = \sigma^0 / \sqrt{3}$. The plastic parameters of the yarns in the unaged and aged composites are listed in Table 3.

The ductile and shear damage criteria and damage evolution which was based on energy to define the damage of resin and yarns were used in FEA. The state variables ω_i (ω_D and ω_S) of damage initiation can be written as Eq. (6).

$$\omega_i = \int \frac{d\bar{\epsilon}^{pl}}{\bar{\epsilon}_i^{pl}(\sigma_i, \bar{\epsilon}^{pl})} = 1, (i=D, S) \quad (6)$$

where $\bar{\epsilon}^{pl}$ is the equivalent plastic strain. The damage and shear will happen when it reaches up to the $\bar{\epsilon}_D^{pl}$ and $\bar{\epsilon}_S^{pl}$. σ_S is the shear stress ratio,

and σ_D is the stress triaxiality as shown in Eq. (7).

$$\sigma_D = \frac{\sqrt{2}}{3} \times \frac{\sigma_1 + \sigma_2 + \sigma_3}{(\sigma_1 - \sigma_2)^2 + (\sigma_2 - \sigma_3)^2 + (\sigma_3 - \sigma_1)^2} \quad (7)$$

The stiffness constants will degrade in terms of Eq. (8). Where $\bar{\sigma}$ is the undamaged stress tensor, and D is the damage variable which will range from 0 to 1 with damage and failure appearing. The element will be eliminated when the materials are completely damaged.

$$\sigma = (1 - D) \bar{\sigma} \quad (8)$$

Furthermore, interface between yarns and resin is a crucial part of composites. The thermal oxygen ageing will induce interface debonding, which results in the mechanical properties decreasing. In this paper, the surface-based cohesive zone model was used to define interface properties according to bilinear traction-separation law. Before debonding, the interface properties show linear elastic response as follows:

$$\mathbf{T} = \begin{Bmatrix} T_n \\ T_s \\ T_t \end{Bmatrix} = \mathbf{K} \delta = \mathbf{K} \begin{Bmatrix} \delta_n \\ \delta_s \\ \delta_t \end{Bmatrix} \quad (9)$$

\mathbf{T} and δ represent interface stress and relative displacement respectively. n , s and t are the three directions in three degrees of freedom at each node, i.e., n stands for the normal, and s , t for tangential. \mathbf{K} is the initial modulus of the interface.

Maximum nominal stress criterion and Benzeggagh Kenane (B-K) fracture criterion was used to control damage initiation and evolution process of the interface. The maximum nominal stress values including normal only (σ_n), shear-1 only (σ_s) and shear-2 only (σ_t) are listed in Table 4. The B-K criterion is given as follows:

$$G^C = G_n^C + (G_s^C - G_t^C) \left\{ \frac{G_s + G_t}{G_s + G_n} \right\}^\eta \quad (10)$$

G^C represents critical fracture energies. η is the viscosity coefficient. The interface parameters are listed in Table 4. The weakness of interface parameters method was used to indicate the properties of the aged composites.

Fig. 5(c) shows the mesh size sensibility of composites with 15° under impact along IP direction. When the mesh size is higher than 0.3 mm, the elastic modulus and peak stress values in FEA are larger than those in experiment. When it is lower than 0.3 mm, the elastic modulus and peak stress values in FEA are more consistent with experiment. The mesh size and element types of yarns, impact plate, supporter and resin were listed in Table 5.

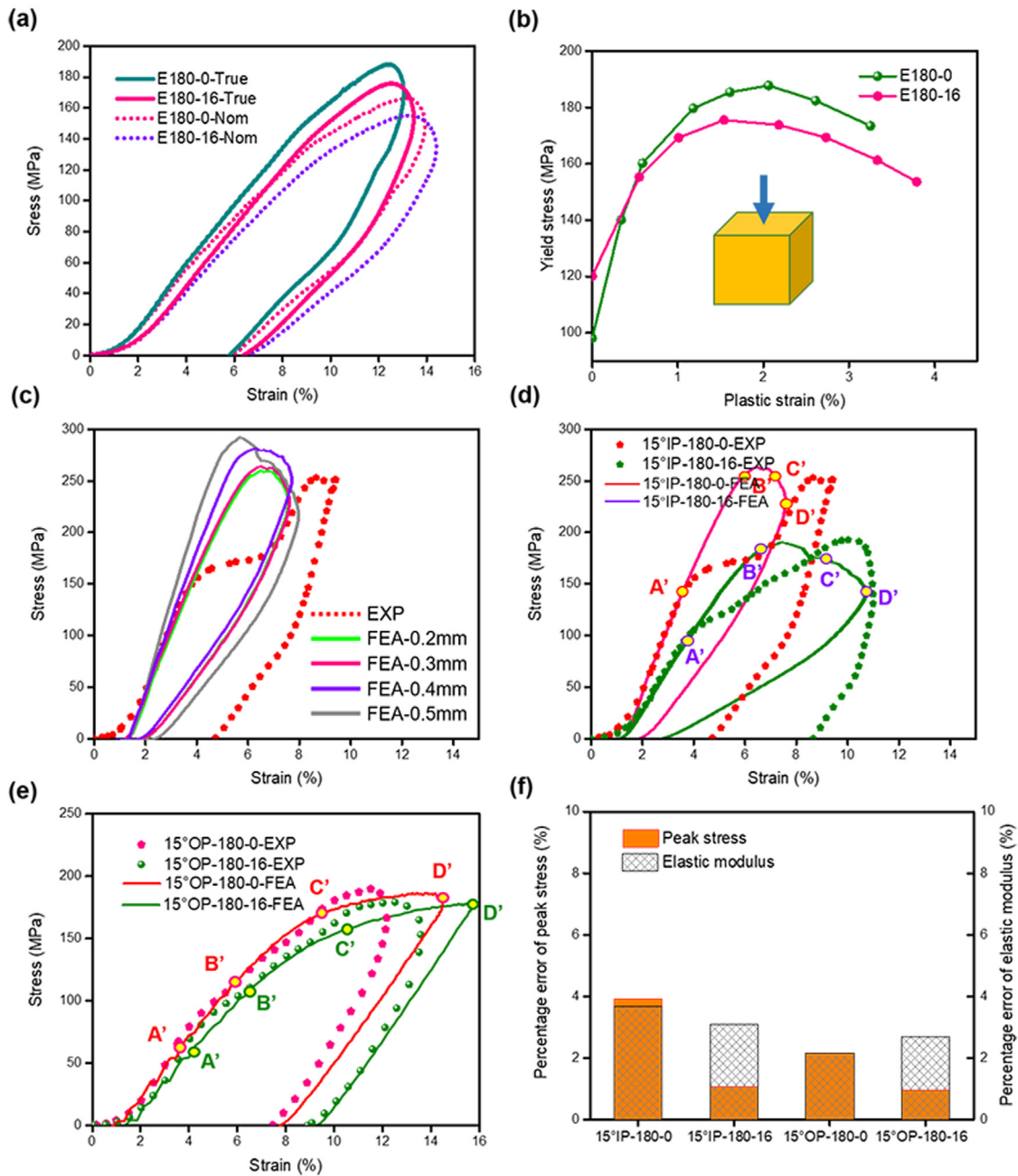


Fig. 5. The plastic parameters of neat epoxy resin and verify of stress–strain behaviors in unaged and aged composites along IP and OP loadings between experiment (EXP) and FEA, (a) nominal and true stress–strain curves, (b) yield stress–plastic strain curves, (c) mesh size sensitive, (d) stress–strain curves along IP direction, (e) stress–strain curves along OP, (f) percentage errors of peak stress and elastic modulus between EXP and FEA.

Table 4
The interface parameters of unaged and aged composites.

	K_n (N/mm ³)	$K_s = K_t$ (N/mm ³)	σ_n (MPa)	$\sigma_s = \sigma_t$ (MPa)	G_n^C (N/mm)	$G_s^C = G_t^C$ (N/mm)	η
Unaged	4×10^6	1×10^6	120	150	0.25	1.0	1.0
Aged	2.67×10^6	6.67×10^5	60	75	0.54	0.8	1.0

Fig. 5(d) and (e) compare the experimental stress–strain results (EXP) of the unaged and the aged composites with those of FEA along IP and OP directions respectively. Most of the loading portion is captured accurately, while significant differences in the stress or strain where the maximum occurs and in the unloading part of the curve are observed. Especially in IP loading case, there is no additional yield stage in the FEA results before the peak stress because the composites are considered to uniformly deforming during impact. While in experiment

condition, the stress along IP direction is sensitive to sample regularity which will induce larger concentration of deformation and damages as shown in Section 3.3. Additionally, the plastic strain values in the unloading part of EXP curves are higher than those in the FEA. In the experimental tests, the uneven cross-section results in external deformation and damages during loading. Especially in the FEA of the aged composites, the stress reduces once damage occurs. The more damages propagate along the horizontal direction because of the existed ageing

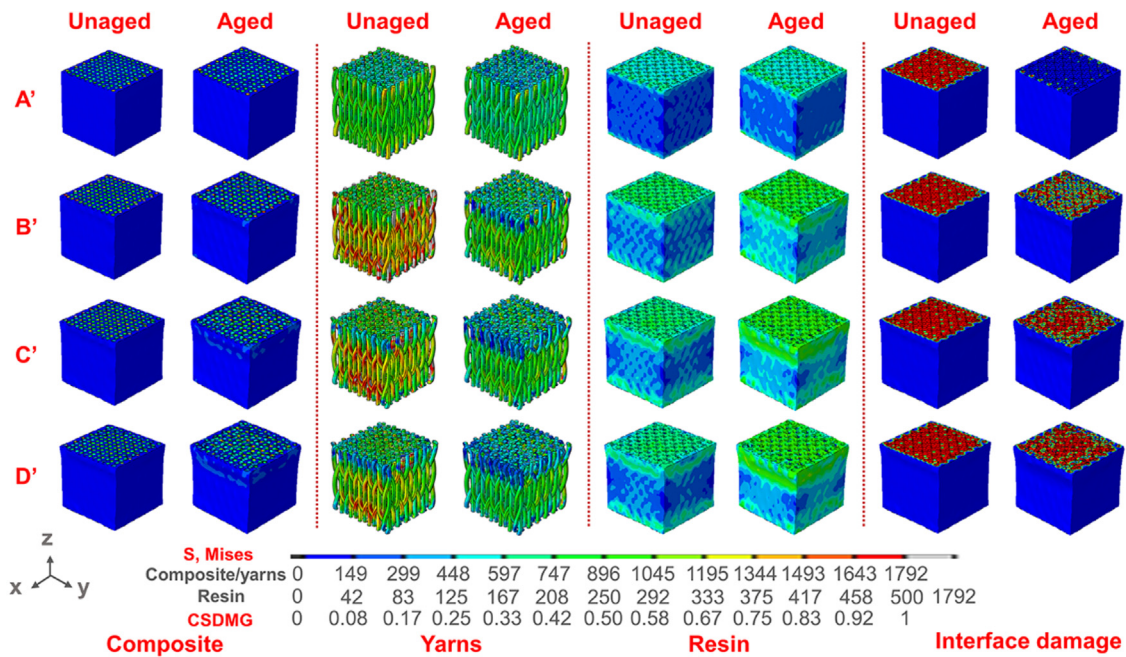


Fig. 6. The global stress distribution and interface damages in unaged and aged composites during IP loading by FEA.

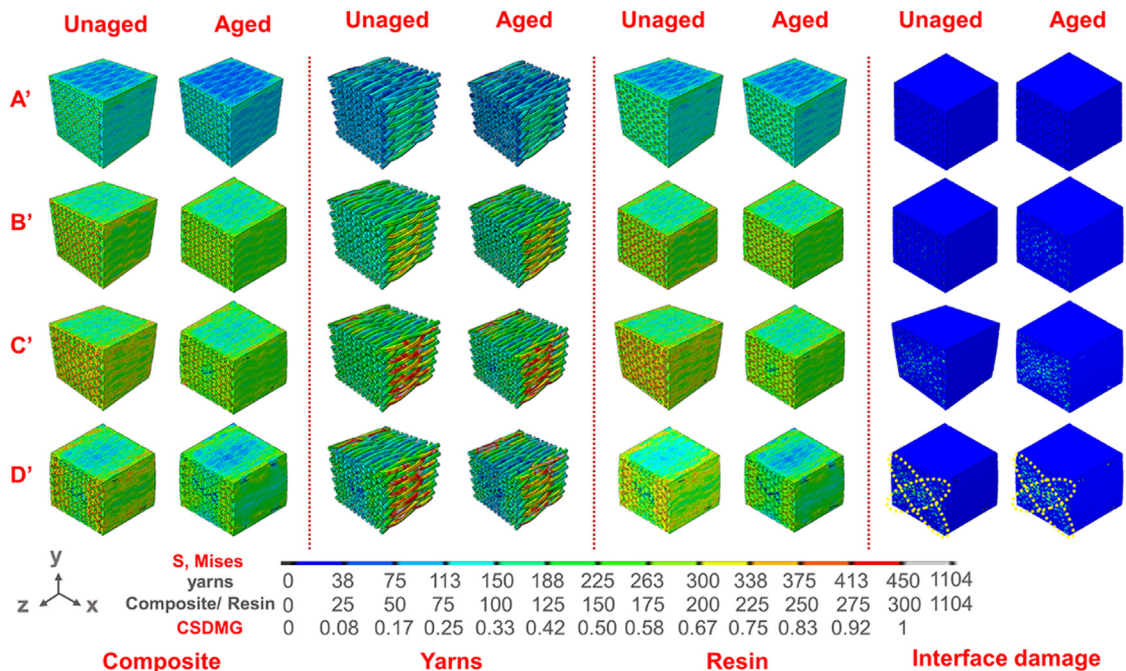


Fig. 7. The global stress distribution and interface damages in unaged and aged composites during OP loading by FEA.

Table 5

The mesh size and element types of geometrical model.

	Yarns	Impact plate/Rigid supporter	Resin
Element type	C3D8R	C3D8R	C3D4
Mesh size (mm)	0.3	2.5	0.3
Element number	14958	809	288893

cracks, which leads to the lesser plastic deformation and more energy converts to elastic strain. In addition, ageing crack morphology effect was ignored in the FEA. The percentage errors of peak stress and elastic modulus between FEA and EXP are shown in Fig. 5(f), which are all

lower than 4%. The four specific points were used to analyze damage process such as A', B', C' and D', which means zero damage at 1/2 strain position of elastic stage, initial damage, midpoint between initial damage and max strain, and max strain, respectively.

3.2.2. Spatial stress and damage distributions during loading

Figs. 6–9 display global, 1/2 and 1/4 position along y axial stress distribution in composites, yarn and epoxy matrix and interface damage (CSDMG, the 0–1 represents gradual increase in damage degree) during IP and OP loading at A', B', C' and D' positions. The color distribution indicates that carbon fiber tows carry most of compressive stress with the loading going on. The stress of the outermost surface yarn is higher

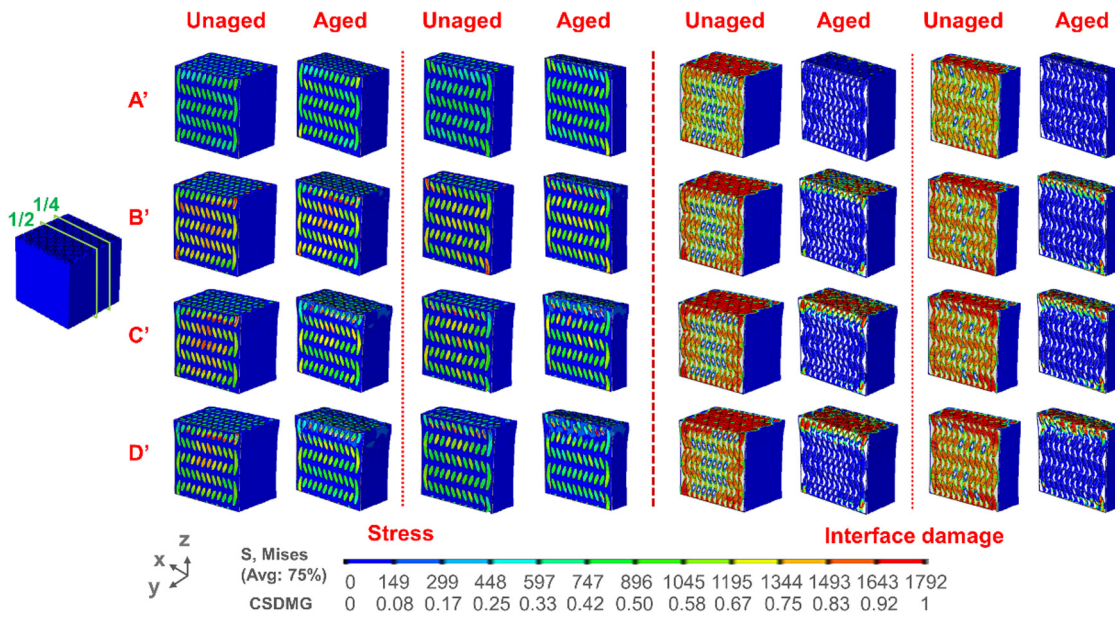


Fig. 8. The stress distribution and interface damages in unaged and aged composites at 1/2 and 1/4 positions along y direction along IP impact.

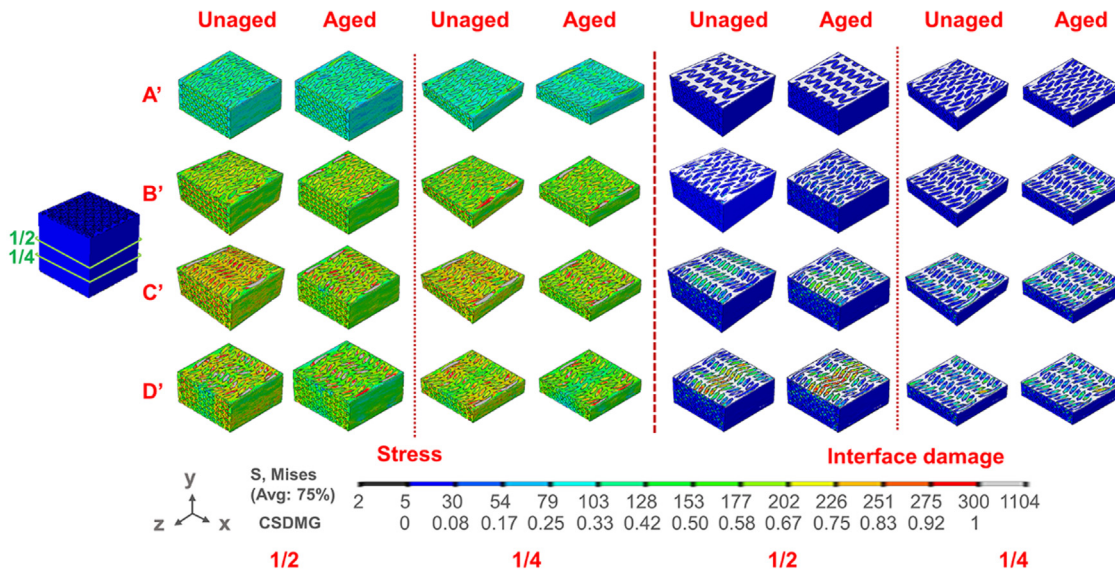


Fig. 9. The stress distribution and interface damages in unaged and aged composites at 1/2 and 1/4 positions along y direction along OP impact.

than that of interior in IP loading due to the surface yarns are more parallel to loading direction than that of interior region (Fig. 4). The stress distribution images along 1/2 and 1/4 position further manifest that multiple interface damages of the unaged composites extend from load end to bottom side in surrounding area, which is more than a quarter area. Correspondingly, the interior area bears more stress than the surrounding area due to cracks could hinder stress waves propagating. Different from the evolution process in the unaged composite, the interface damages of the aged composite mainly focus on load side, and lesser propagates inward, while more horizontal extension occurs. Along OP direction, the stress wave transfers from surface resin which touched with impact plate to yarn through the interface during impact loading, gradually forming X-shape shear band. Yarns and resin share the impact loads together. The inner interface damage appears on center location of sample and spreads out along X-shape (Fig. 7), which is no more than a half area of composites as shown in Fig. 9 marked in red. Anisotropy of reinforcement results in different interaction among yarns when suffered from loads in different direction.

Fig. 10 shows yarn selection and stress comparison along the same yarn at D' under IP and OP loading. The selected yarn should span surrounding damage area in IP loading and interior area in OP. The 18 nodes were chosen to compare stress values. It can be seen that stress values are all different, and that in IP case are higher than that in OP, which induced by the higher carrying load capacity of the axial carbon fiber tows. The fluctuation of stress curve at both ends of yarn in the IP directions were due to the points located in surrounding damage area. The stress of the interior region of the unaged composites is obvious higher than that in the aged sample along IP directions, while it has little difference in OP direction because the damage is in dispersed distribution along this yarn.

In addition, the CSDMG and Mises stress values are shown at A', B', C' and D' along the same path and section (Figs. 11(a-e) and 12(a-e)). As load goes on, the interface at some locations begin to weak at B' point and appear to complete failure at D' (marked with green ellipse dotted box). The corresponding stresses decrease after interface weakness (B'). For IP loading, interface debonding distributes on some

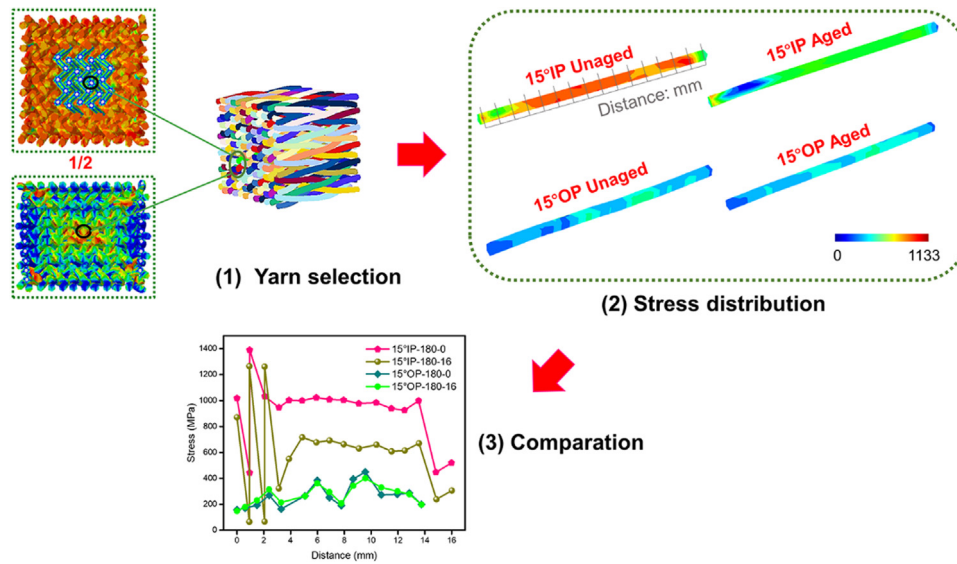


Fig. 10. The Mises stress values along the same yarn at D' (maximum strain point) in composites along IP and OP loading.

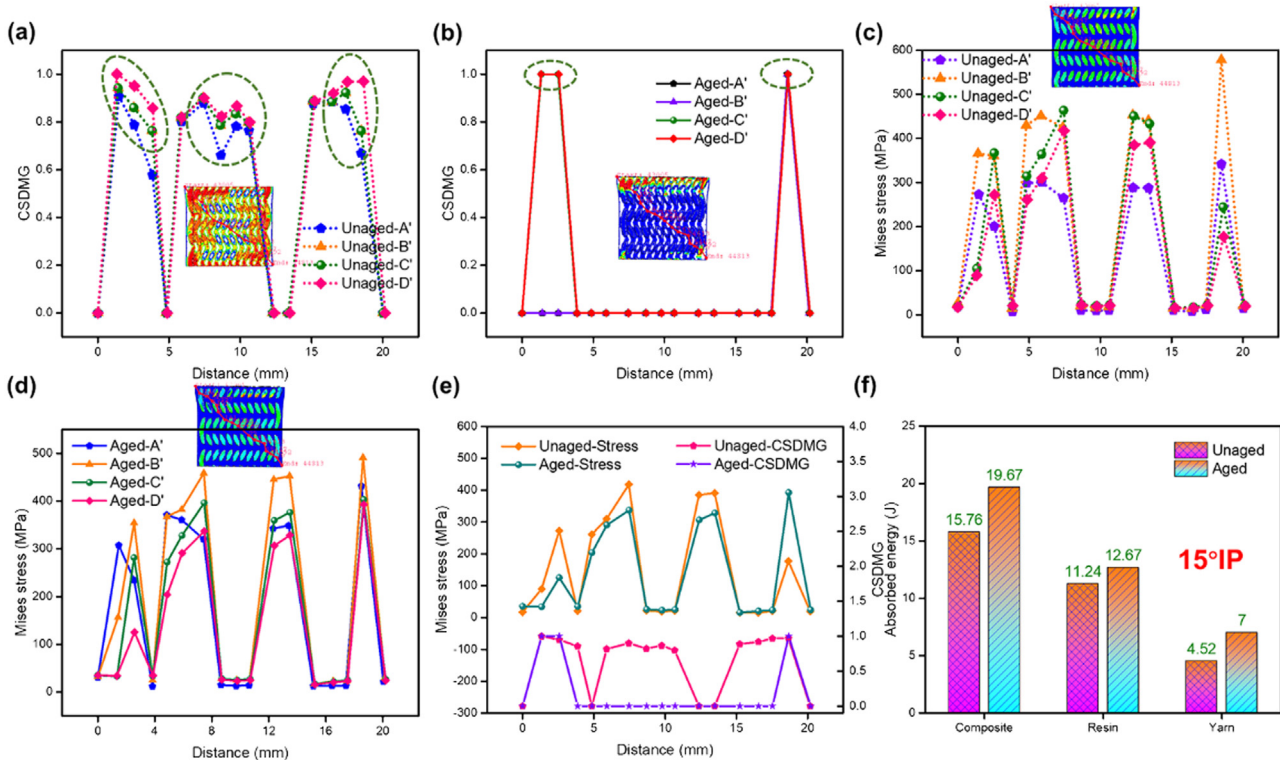


Fig. 11. (a)–(e) The CSDMG and stress values of unaged and aged composites along specific path in IP loading by FEA, (f) final absorbed energy.

positions at both ends in path. Especially, the more serious damages near loading end in the aged composites result in no damages in the middle of path. The interfacial damage occurs along entire path in the OP direction, while debonding mainly distributes on middle section. Figs. 11(e) and 12(e) compare the values of stress and CSDMG in the unaged sample with that at D' location along IP and OP directional impacts. It is obvious that stresses of the unaged composites are higher than that of the aged sample, and the interface damage results in stress degradation. All energy totals of composite, yarn and resin matrix (Figs. 11(f) and 12(f)) were extracted in the FEA results. The results indicate that resin absorbs major energy in the unaged and aged composites, which are 11.24 J and 12.67 J in IP, 19.98 J and 20.71 J in OP, occupied 71.32% and 64.41%, 98.23% and 99.04%, respectively.

3.3. The damage evolution and failure during loading

3.3.1. Damage morphology

The damage evolution mode is difficult to be identified along OP direction due to limited resolution of current camera. It has been discussed based on scanning electron microscopy (SEM) images in Section 3.4. Fig. 13 shows the damage morphologies of 15°, 25° and 35° angle composites in the process of IP loading. The A–E points were signed on stress–strain curves as shown in Fig. 2, in which means zero damage at 1/2 strain position of elastic stage, initial damage, midpoint between initial damage and max stress, max strain, and zero stress point at last, respectively. The detailed description about the whole damage

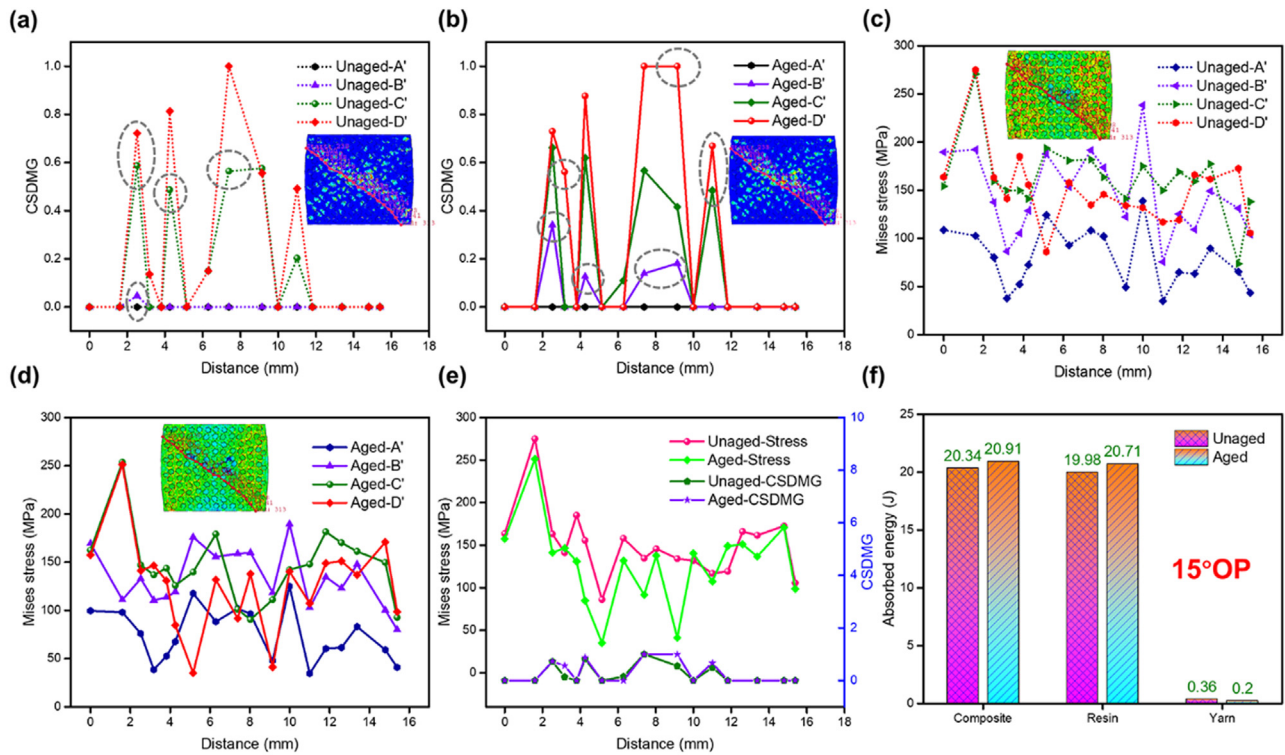


Fig. 12. (a)–(e) The CSDMG and stress values of unaged and aged composites along specific path along OP loading by FEA, (f) final absorbed energy.

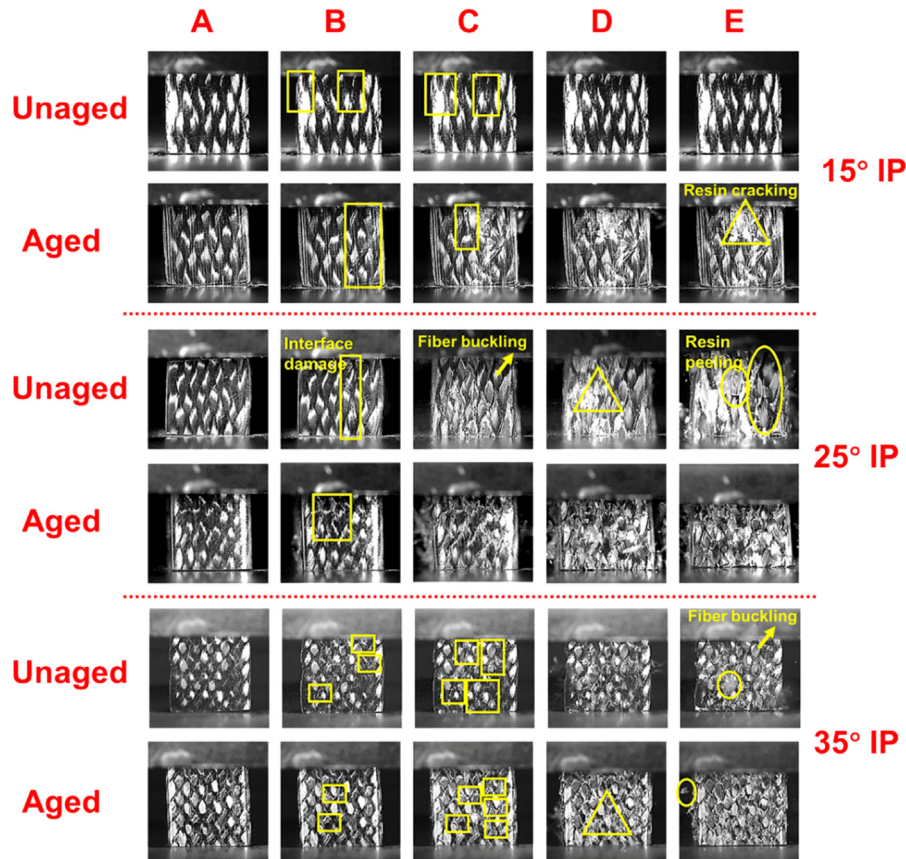


Fig. 13. The damage and failure morphology evolutions of unaged and aged composites with surface braided angles of 15°, 25°, 35° during IP loading.

process of the 25° composites which include interface debonding, resin cracking and peeling, fiber bulking and slippage, can refer to our

previous work [26]. It is worth noting that the damages of the 15° composites in experimental are more serious than that in FEA because

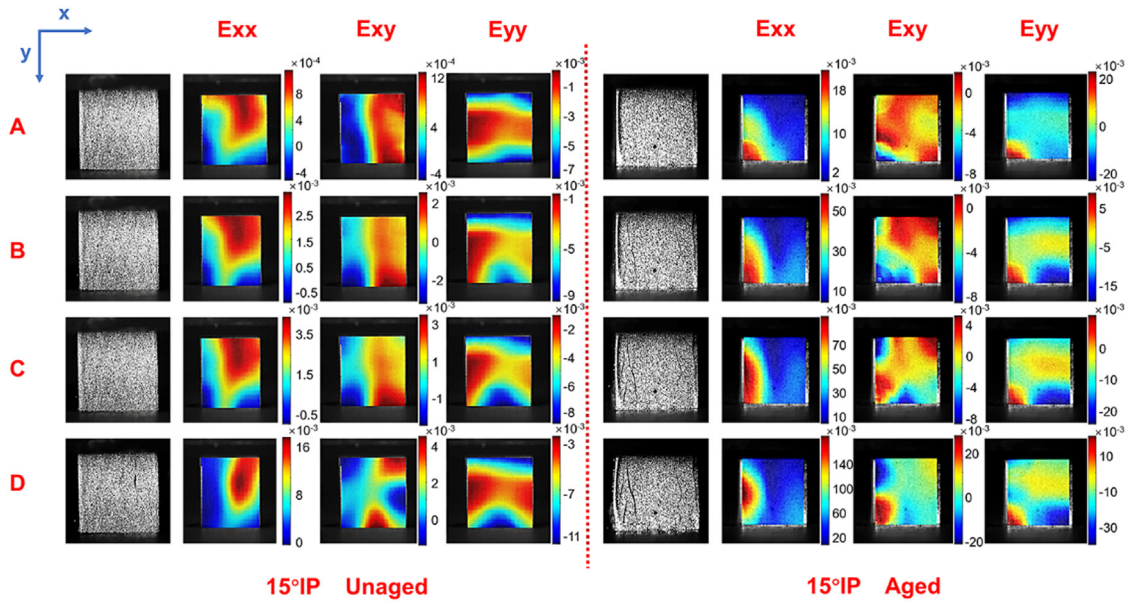


Fig. 14. The local strain distribution of unaged and aged composites with 15° along IP loading.

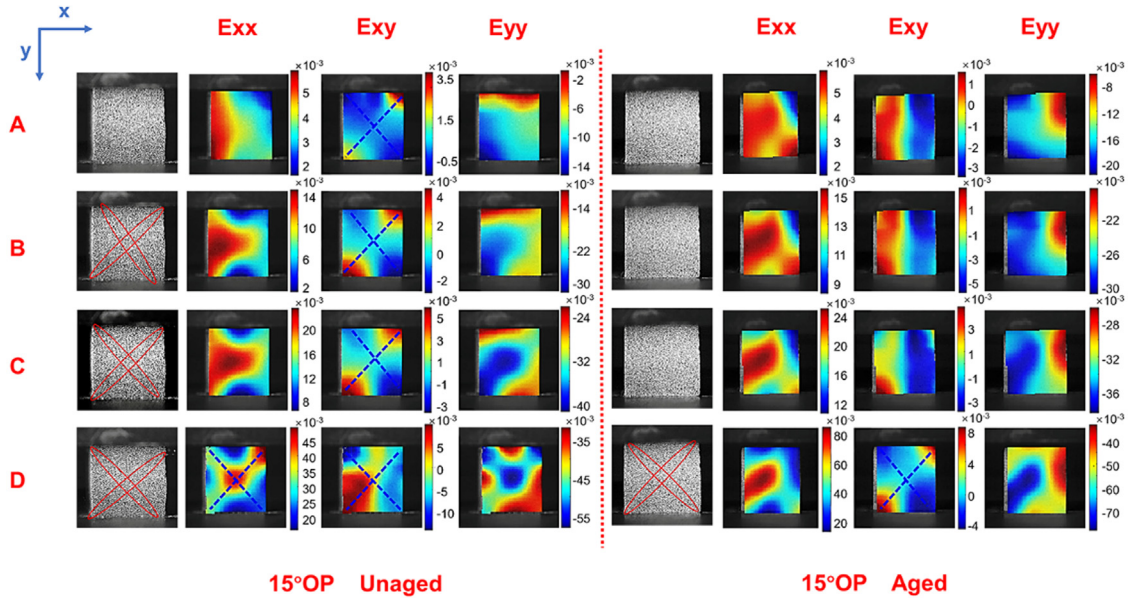


Fig. 15. The local strain distribution of unaged and aged composites with 15° along OP loading.

that it is prone to interface cracking induced by stress concentration between high and low plane in experiment, while the structure in FEA is neat. The rules of damage initiation and propagation are consistent in the 15°, 25° and 35° composites with the loading going on, only damage modes in 15° are different which only include interface cracking and matrix cracking. There are more interface damages in the 35° composites due to more braided cycles which induced more interface sites. While the deformation is lesser than that of the 25° sample after ageing. That indicates that the compact structure contributes to resistance to deformation during impact loading. Furthermore, the damages in the aged composite are all greater than those of the unaged samples.

3.3.2. Local strain distribution

Figs. 14 and 15 show local strain evolution of unaged and aged composites with 15° angle under IP and OP loading. Tensile strain appears in the x direction ($E_{xx} > 0$). Strain appears in the y directions

($E_{yy} < 0$), while E_{yy} is greater than zero when surface resin occurs local damages such as behavior in aged composite under IP loading. Shear strain (E_{xy}) depends on the E_{xx} and E_{yy} . The values of E_{xx} and E_{yy} in aged are higher than that in unaged, and show local increase feature with loading processing. Generally, there is strain concentration at damage area. The X-shape shear strain bands occur in unaged composites during OP loading, and it begins to exist after D point in aged composites which is affected by ageing cracks. That illustrates that ageing cracks will affect local strain distribution.

3.4. The final damage and failure morphology

Fig. 16(a) and (b) show final failure morphologies on global and cross-section of 3D braided composites with 15°, 25° and 35° angles along IP and OP directional impact. There is almost invisible damage in the 15° sample along the OP impact. Whereas interface debonding could be observed at diagonal of cross-section in the unaged sample

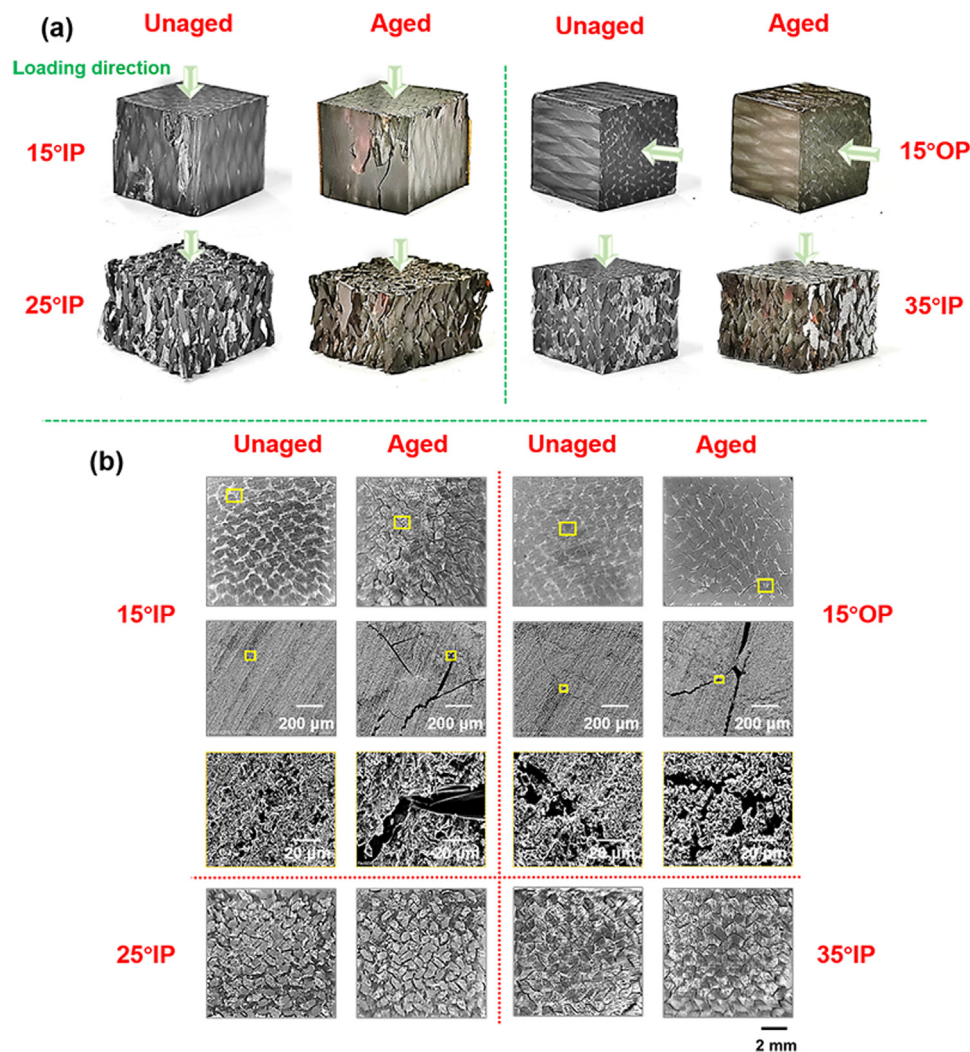


Fig. 16. The final failure morphologies of unaged and aged composites with different braided angles along IP and OP loading, (a) global morphologies, (b) cross-section morphologies.

using scanning electron microscopy (SEM). The more cracks appear in the aged composites because of the integrate effects of the ageing and the impact loading. It indicates that the interface debonding is the main damage mode during LVI along OP direction. In the IP directional loading, there are lesser interface cracks on cross-section of the unaged 15° composites, and the width of some cracks in the aged samples is greater than that along OP direction. Some surface resin falls off under impact. The interface debonding and resin falling off in composites before and after ageing are the main damage modes. In the 25° composites loading, the thermal oxygen ageing only changed the crack propagation path but not the damage modes such as matrix cracking, interface cracking, matrix fracture and peeling off, fiber buckling and slipping, and fiber breakage [26]. The tighter structure in 35° composites reduced the deformation during impact. There is no fiber breakage damage. In addition, the damage modes and ageing effect on it are the same with those in the 25° composites.

4. Conclusions

The low-velocity impact behaviors of 3D braided composites along in-plane and out-of-plane directions after thermo-oxidative ageing were investigated. The stress-strain behaviors, stress and damage distributions, macroscopic and microscopic failure morphologies were discussed based on test and FEA results. The results indicated that the ultimate strength and stiffness degradation are sensitive to loading

direction, which are 23.79% and 28.73% in IP direction, and 5.6% and 8.55% in OP direction, respectively. With impact along IP direction, the damages mainly propagate to interior along surrounding area and yarn path in unaged composites, while they mainly distribute on the top of load side and extend in horizontal direction. The higher stress mainly distributes on interior regions and braided yarns. However, shear damages form X-shape band at diagonal of cross-section in OP direction, and yarn and resin matrix share the impact loads. The braided angles effects on the ageing degradation along IP directional impact were also discussed. The results indicate that the braided composites with larger angles contributed to higher mechanical properties retention when suffered from high temperature and oxygen ageing, while the damage modes did not change.

CRediT authorship contribution statement

Yuanyuan Wu: Writing – original draft, Investigation, Data curation. Jinhui Guo: Data curation. Limeng Xun: Formal analysis. Baozhong Sun: Project administration. Bohong Gu: Writing – review & editing, Methodology, Funding acquisition.

Declaration of competing interest

The authors declare that they have no known competing financial interests or personal relationships that could have appeared to influence the work reported in this paper.

Data availability

Data will be made available on request.

Acknowledgments

This work was supported by the National Science Foundation of China (Grant Number 51875099), and the Fundamental Research Funds for the Central Universities and Graduate Student Innovation Fund of Donghua University, China (Grant Number CUSF-DH-D-2022022). The project was funded by Shanghai Frontier Science Research Center for Modern Textiles, Donghua University.

References

- [1] M. Hu, B. Sun, et al., Microstructure modeling multiple transverse impact damages of 3-D braided composite based on thermo-mechanical coupling approach, *Compos. B Eng.* 214 (2021) 108741, <http://dx.doi.org/10.1016/j.compositesb.2021.108741>.
- [2] D.S. Li, W.F. Han, et al., On the tensile properties and failure mechanisms of 3D six-directional braided composites at elevated temperatures, *Compos. Commun.* 28 (2021) 100884, <http://dx.doi.org/10.1016/j.coco.2021.100884>.
- [3] K.L. Xu, W. Chen, et al., Longitudinal compressive property of three-dimensional four-step braided composites after cyclic hygrothermal aging under high strain rates, *Appl. Sci. Basel* 10 (2020) 2061, <http://dx.doi.org/10.3390/app10062061>.
- [4] M. Zhang, B. Sun, et al., Meso-structure ageing mechanism of 3-D braided composite's compressive behaviors under accelerated thermo-oxidative ageing environment, *Mech. Mater.* 115 (2017) 47–63, <http://dx.doi.org/10.1016/j.mechmat.2017.09.002>.
- [5] S. Liu, J. Zhang, et al., Damage and failure mechanism of 3D carbon fiber/epoxy braided composites after thermo-oxidative ageing under transverse impact compression, *Compos. B Eng.* 161 (2019) 677–690, <http://dx.doi.org/10.1016/j.compositesb.2018.11.140>.
- [6] B. Sun, B. Gu, High strain rate behavior of 4-step 3D braided composites under compressive failure, *J. Mater. Sci.* 42 (2007) 2463–2470, <http://dx.doi.org/10.1007/s10853-006-1295-x>.
- [7] D. Li, Y. Yang, et al., Experimental study on the fabrication, high-temperature properties and failure analysis of 3D seven-directional braided composites under compression, *Compos. Struct.* 268 (2021) 113934, <http://dx.doi.org/10.1016/j.compstruct.2021.113934>.
- [8] C. Cui, J. Dong, et al., Effect of braiding angle on progressive failure and fracture mechanism of 3-D five-directional carbon/epoxy braided composites under impact compression, *Compos. Struct.* 229 (2019) 111412, <http://dx.doi.org/10.1016/j.compstruct.2019.111412>.
- [9] A. Singh, N. Reynolds, et al., The effect of braid angle on the flexural performance of structural braided thermoplastic composite beams, *Compos. Struct.* 261 (2021) 113314, <http://dx.doi.org/10.1016/j.compstruct.2020.113314>.
- [10] X.Z. Gao, A. Siddique, et al., Influence of braiding angle on multiple impact damages of 3-D braided composite along longitudinal direction, *Appl. Compos. Mater.* 26 (2019) 1261–1280, <http://dx.doi.org/10.1007/s10443-019-09779-1>.
- [11] Z. Zhao, L. Liu, et al., Dynamic compressive behavior in different loading directions of 3D braided composites with different braiding angle, *Lat. Am. J. Solids Struct.* 15 (2018) e109, <http://dx.doi.org/10.1590/1679-78255111>.
- [12] K. Luan, J. Liu, et al., High strain rate compressive response of the C-f/SiC composite, *Ceram. Int.* 45 (2019) 6812–6818, <http://dx.doi.org/10.1016/j.ceramint.2018.12.174>.
- [13] Y. Wu, L. Xun, et al., Crack spatial distributions and dynamic thermomechanical properties of 3D braided composites during thermal oxygen ageing, *Compos. A-Appl. Sci. Manuf.* 144 (2021) 106355, <http://dx.doi.org/10.1016/j.compositesa.2021.106355>.
- [14] A.El. Mourid, R. Ganesan, et al., Anisotropic oxidation due to aging in a triaxially braided composite and its influence on tensile failure, *Compos. B Eng.* 76 (2015) 1–12, <http://dx.doi.org/10.1016/j.compositesb.2014.12.006>.
- [15] H.-m. Zuo, H. Zhu, et al., Study on in-plane compression properties and numerical modeling of three dimensional five-directional braided composites, *Thin-Walled Struct.* 168 (2021) 108232, <http://dx.doi.org/10.1016/j.tws.2021.108232>.
- [16] X.F. Lou, H.N. Cai, et al., Failure analysis of composite laminate under low-velocity impact based on micromechanics of failure, *Compos. Struct.* 163 (2017) 238–247, <http://dx.doi.org/10.1016/j.compstruct.2016.12.030>.
- [17] H. Singh, K.K. Namala, et al., A damage evolution study of E-glass/epoxy composite under low velocity impact, *Compos. B Eng.* 76 (2015) 235–248, <http://dx.doi.org/10.1016/j.compositesb.2015.02.016>.
- [18] Y. Hu, W. Liu, et al., Low-velocity impact damage research on CFRPs with Kevlar-fiber toughening, *Compos. Struct.* 216 (2019) 127–141, <http://dx.doi.org/10.1016/j.compstruct.2019.02.051>.
- [19] Y. Hu, Y. Shi, et al., Damage tolerance of 2-dimensional UHMWPE/CF hybrid woven laminates subjected to low-velocity impact, *Mater. Des.* 191 (2020) 108604, <http://dx.doi.org/10.1016/j.matdes.2020.108604>.
- [20] Y. Hu, D. Liu, et al., Low-velocity impact damage research on 2-dimensional UHMWPE/CF hybrid woven laminates under preloading, *Thin-Walled Struct.* 161 (2021) 107472, <http://dx.doi.org/10.1016/j.tws.2021.107472>.
- [21] Y. Hu, Y. Shi, et al., Low-velocity impact damage tolerance of ultrahigh molecular weight polyethylene/carbon fiber laminates under prestress, *Polym. Compos.* 43 (2022) 712–729, <http://dx.doi.org/10.1002/pc.26404>.
- [22] Q. Gu, Z. Quan, et al., Structural modeling and mechanical characterizing of three-dimensional four-step braided composites: A review, *Compos. Struct.* 207 (2019) 119–128, <http://dx.doi.org/10.1016/j.compstruct.2018.09.065>.
- [23] B. Shi, M. Zhang, et al., Multi-scale ageing mechanisms of 3D four directional and five directional braided composites' impact fracture behaviors under thermo-oxidative environment, *Int. J. Mech. Sci.* 155 (2019) 50–65, <http://dx.doi.org/10.1016/j.ijsmecsci.2019.02.040>.
- [24] J. Blaber, B. Adair, et al., Ncorr: Open-source 2D digital image correlation matlab software, *Exp. Mech.* 55 (2015) 1105–1122, <http://dx.doi.org/10.1007/s11340-015-0009-1>.
- [25] D. Zhang, X. Zheng, et al., Effects of braiding architectures on damage resistance and damage tolerance behaviors of 3D braided composites, *Compos. Struct.* 232 (2020) 111565, <http://dx.doi.org/10.1016/j.compstruct.2019.111565>.
- [26] Y.Y. Wu, W.J. Cao, et al., Near-fiber nanomechanical mapping and impact failure mechanism of 3D braided composites subjected to thermo-oxidative environment, *Compos. Sci. Technol.* 216 (2021) 109052, <http://dx.doi.org/10.1016/j.compscitech.2021.109052>.
- [27] D. Zhang, Y. Sun, et al., Prediction of macro-mechanical properties of 3D braided composites based on fiber embedded matrix method, *Compos. Struct.* 134 (2015) 393–408, <http://dx.doi.org/10.1016/j.compstruct.2015.08.088>.
- [28] W. Cao, J. Zhang, et al., X-ray tomography and numerical study on low-velocity impact damages of three-dimensional angle-interlock woven composites, *Compos. Struct.* 230 (2019) 111525, <http://dx.doi.org/10.1016/j.compstruct.2019.111525>.
- [29] M. Zhang, C. Zuo, et al., Thermal ageing degradation mechanisms on compressive behavior of 3-D braided composites in experimental and numerical study, *Compos. Struct.* 140 (2016) 180–191, <http://dx.doi.org/10.1016/j.compstruct.2016.01.029>.
- [30] B. Shi, S. Liu, et al., Comparisons on impact fracture behavior between three-dimensional four directional and five directional braided composite materials, *Int. J. Damage Mech.* 28 (2018) 990–1020, <http://dx.doi.org/10.1177/1056789518805218>.
- [31] H. Huang, A.M. Waas, Compressive response of Z-pinned woven glass fiber textile composite laminates: Modeling and computations, *Compos. Sci. Technol.* 69 (2009) 2338–2344, <http://dx.doi.org/10.1016/j.compscitech.2009.01.008>.
- [32] Z.M. Huang, A bridging model prediction of the ultimate strength of composite laminates subjected to biaxial loads, *Compos. Sci. Technol.* 64 (2004) 395–448, [http://dx.doi.org/10.1016/S0266-3538\(03\)00220-3](http://dx.doi.org/10.1016/S0266-3538(03)00220-3).